

Supporting Information

Sulfonated ultramicroporous membrane with selective ion transport enables osmotic energy extraction from multiform salt solutions with exceptional efficiency

Qing Zhu, Yuanyuan Li, Qingling Qian, Peipei Zuo, Michael D Guiver, Zhengjin Yang, and Tongwen Xu

Abstract:

Osmotic power that can be converted into electricity in membrane-based processes, is a sustainable energy source. This concept is, however, limited to salinity differences between seawater and river water, while the efficiency is often restrained by inadequate membrane selectivity. We propose by confining the transport of ions within the <1 nm sized ion channels, high membrane selectivity can be acquired, thereby improving osmotic power generation and extending the concept to other solutions, e.g. industrial wastewater. This is demonstrated with an intrinsically ultramicroporous sulfonated polyanthene-based (SPX) membrane. The SPX membrane with negatively charged sub-1-nm channels shows charge-governed ion transport and strong size effect, which combine to contribute high selectivity. Osmotic power generator with the SPX membrane delivers an efficiency of 38.5% from mixing river water with seawater. The strong size effect also enables power generation from solutions with equimolar concentrations, a conceptually new energy extraction system. Combining concentration and thermal gradients yields a power output of 1.2 W m⁻², along with an exceptional efficiency of 48.7%. The results highlight the potential of the proposed membrane in energy-harvesting devices and open unexplored avenues towards diversified forms of osmotic electricity generation.

Experimental section

Materials.

Anodic aluminum oxide (AAO) membrane was purchased from Hefei Puyuan Nanotechnology Co., Ltd. (Hefei, P.R. China). Sulfonated poly (2,6-dimethyl-1,4-phenylene oxide) (SPPO) was manufactured by Hefei ChemJoy® Polymer Materials Co., Ltd (Anhui, P.R. China). Other chemicals were of analytical grade, purchased from domestic chemical suppliers, and used as received.

Synthesis of Sulfonated Polymers.

The SPX polymer was synthesized through superacid catalyzed polymerizations using commercially available monomer 4,4'-dihydroxybiphenyl according to a reported procedure.¹ The resulting polymers with high molecular weight are readily soluble in polar organic solvents for casting mechanically robust membranes.

Fabrication of SPX membrane.

The SPX polymer was dissolved in dimethyl sulfoxide (DMSO). The resultant polymer solutions were poured into glass Petri dishes and placed on a heating plate at 60 °C over a few days until the solvent completely evaporated. The resulting free-standing membrane was then peeled off from the glass Petri dish and vacuum dried overnight. The thickness of free-standing SPX membrane samples was controlled at about 30 μm. The degree of sulfonation or the sulfonic moiety content, that is, ion exchange capacity (IEC, mmol g⁻¹) as determined by titration can be tuned by controlling the reaction time or the amount of chlorosulfonic acid used. The IEC value of SPX membrane used in this work was controlled at ~ 0.95 mmol g⁻¹. The SPX membrane with a relatively higher IEC of 0.95 mmol g⁻¹ show significantly improved a proton conductivity of 180 mS cm⁻¹ at 80 °C and demonstrates a bulk water uptake of around 30 wt% at all operating temperatures.¹ The SPX membrane has ultramicroporous pores in the size of 5 to 9 Å calculated from CO₂ sorption isotherms based on density functional theory (DFT) calculations.¹ The positron annihilation lifetime spectroscopy (PALS) also suggests a subnanometer-sized pore distribution (**Fig. S1**). Other characterization information related to SPX polymer and the resultant membrane can be found in our previous work.¹

Characterizations.

The water contact angle of the SPX membrane was recorded using a static contact angle measurement on SL200B (Solon Tech Co., Ltd, China) at ambient temperature. A deionized water droplet with a volume of about 5 μL was dropped onto the membrane with a micro-syringe. The image of the droplet was recorded and water contact angle was measured from the recorded image. The zeta potential of the SPX membrane was measured on SurPASS 3 (Anton Paar, Austria) with 1 mM KCl as the electrolyte solution. The pH value was adjusted with 0.05 M HCl or 0.05 M NaOH solutions. The cross-section morphology of the membrane was observed with a scanning electron microscope (SU 8220, Hitachi, Japan) at an acceleration voltage of 15 kV. Prior to testing, the samples were first immersed in 0.5 M NaCl solution for 24 h and then washed with deionized water to remove the residual salts. Energy-dispersive X-ray spectroscopy was employed to map the element distribution on the cross-section of the membrane. The positron annihilation lifetime spectroscopy (PALS) was performed at room temperature on a fast-fast coincidence system with a

time resolution of 200 ps in FWHM.² Membranes were cut into $\sim 10 \times 10$ mm and stacked to a total thickness of ~ 2 mm. The ^{22}Na positron source, enveloped by two $7.5 \mu\text{m}$ Kapton foils, was sandwiched between the two membrane stacks. For accuracy, each sample was measured twice under vacuum. The PALS data was analyzed using the CONTIN program.³

Osmotic power generation experiments.

The ionic transport properties and the energy conversion performance of the SPX membrane were measured by using a Keithley 6487 source meter (Keithley, USA) in a diffusion cell. The membrane was fixed between a lab-made two-compartment diffusion cell and the effective membrane area was about 0.2 mm^2 . A pair of agarose potassium chloride Ag/AgCl salt bridge electrodes were placed on both sides and used to apply a voltage bias across the membrane. The energy extraction performance was evaluated by connecting the cell to an adjustable resistance box (Zhengyangxing, Shenzhen, China). For a given resistance (R), the output power density can be calculated as $P = I^2 \times R$, where I is the corresponding current. The compartments of the diffusion cell were filled with chloride salt solutions, sea water or river water. The concentration of natural sea water and river water was checked by an inductively coupled plasma optical emission spectrometry (ICP-OES, Thermo Scientific iCAP 7400, USA) spectrometer. Other chloride salt solutions were prepared with deionized water. The pH values of electrolyte solutions (KCl or NaCl) were adjusted with the corresponding acid or base (HCl/KOH/NaOH).

Electrode calibration

According to the equivalent circuit diagram of the power generation system (Fig. S6a), the osmotic potential across membranes can be described as follows:

$$V_{oc} = E_{redox} + E_{diff} \quad (1)$$

V_{OC} , E_{redox} , and E_{diff} represent the measured potential, the redox potential generated by the unequal chloride concentration at the electrode-solution interface, and the diffusion potential contributed by the ion-selective membrane, respectively.

In this work, the generation of E_{redox} was avoided by connecting the electrode to the cell with agarose salt bridges (5% agarose, 2 M KCl).⁴ This correction can also be made by subtracting the calculated redox potential (Fig. S7b). The theoretical redox potential values were calculated using the Nernst equation.⁵ Results obtained with either method agree well with each other.

Ion mobility measurement

The drift-diffusion experiments were performed to investigate the ion selectivity of the SPX membrane. The two compartments were filled with a series of chloride solutions with fixed concentrations. At a concentration gradient of 10-fold (10 mM/1 mM), I-V curves become shifted along the voltage axis and the corresponding μ^+/μ^- can be estimated from the zero-current potential E_{diff} by the Henderson equation.⁶

$$\frac{\mu^+}{\mu^-} = - \frac{z_+ \ln(\Delta) - z_- FE_{diff}/RT}{z_- \ln(\Delta) - z_+ FE_{diff}/RT} \quad (2)$$

Where z_+ and z_- are the valence of cations and anions, respectively, T is temperature, F is the Faraday constant, R is the universal gas constant, and Δ is the ratio of concentration in two compartments ($\Delta = 10$).

The ion conductivity (σ) was calculated from the slope of the I-V curves as follows :

$$G = \frac{A}{L} \sigma \quad (3)$$

Where G is conductance, A and L are the effective membrane area and thickness of the membrane, respectively.

Conductivity (σ) can be described with the equation below:⁷

$$\sigma \approx F(c_+ \mu^+ + c_- \mu^-) \quad (4)$$

Where c_+ and c_- are the concentration of cations and anions, respectively. Combining the above equation with the found μ^+/μ^- , the values of μ^+ and μ^- for different salts can be deduced.

Energy conversion efficiency

For a given concentration gradient, the cation transference number (t_+) can be described by the following equation:⁸

$$t_+ = \frac{1}{2} \left(\frac{E_{diff}}{RT} \frac{1}{zF \ln \left(\frac{\gamma_{CH} C_H}{\gamma_{CL} C_L} \right)} + 1 \right) \quad (5)$$

Where γ and c represent activity coefficient and concentration of ions; R , T , F , and z refer to the universal gas constant, absolute temperature, Faraday constant, and charge number, respectively.

The energy conversion efficiency is defined as the ratio of the output electrical energy to the input energy (Gibbs free energy of mixing) and has the maximum value of 50%. For a cation-selective system, the maximum power generation efficiency can be calculated as:⁸

$$\eta_{max} = \frac{1}{2} (2t_+ - 1)^2 \quad (6)$$

Molecular simulations

The chain packing model was generated through a 21-step molecular dynamics compression and relaxation procedure⁹ with Gromacs¹⁰⁻¹³ and then visualized with Materials Studio. In the amorphous cell, 6 polymer chains with 20 repeating units were constructed. The swelling effect was considered using the method developed by Colina and coworkers.¹⁴ We generated the swollen model at a swelling degree of 8.3%¹ by expanding the periodic box length to 108.3%. Partial charges were obtained from Gaussian16 calculations at the B3LYP/6-31G(d) level,¹⁵ and other force field parameters were obtained from OPLS_AA force fields. The cutoff radii for vdW and Coulomb interactions were both 10 Å. Particle-mesh Ewald summation method was applied to the long Coulomb interactions. Velocity-rescale and Berendsen algorithm were used to control the temperature and pressure, respectively. A time step of 1.0 fs was used for all the MD simulations. The probe-occupiable volume of different hydrated ions and interconnectivity analysis with a 2.4 Å probe diameter were performed with the software Zeo++.^{16,17}

Figures and Tables

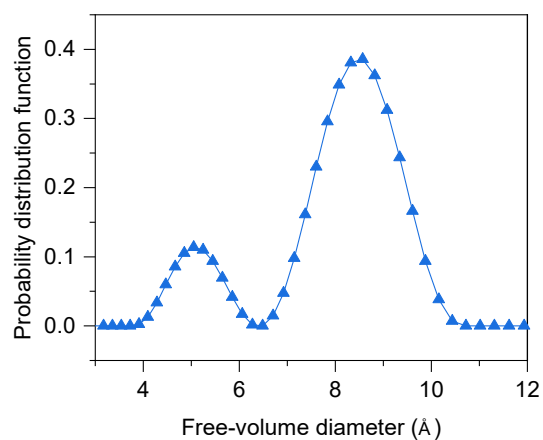


Figure S1. Pore size distribution of the SPX membrane derived from positron annihilation lifetime spectroscopy. Two pore sizes occur at 5 and 8.5 Å and demonstrates the membrane has <1 nm interconnected channels.

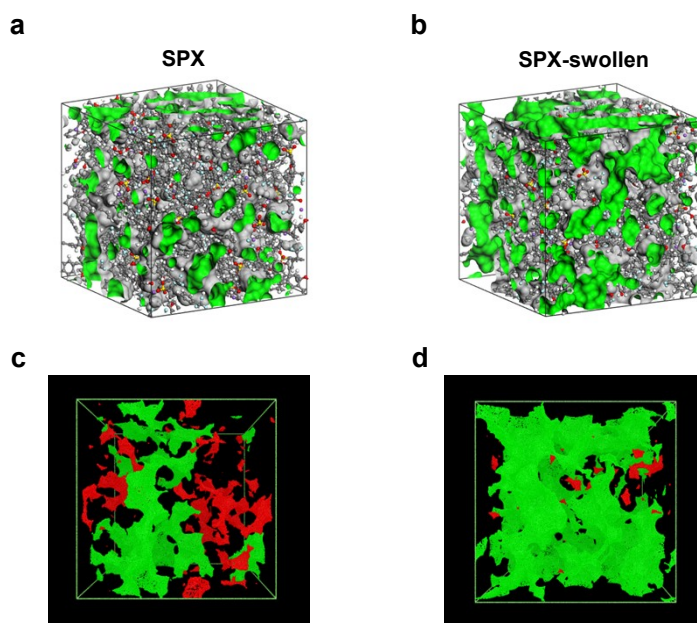


Figure S2. Three-dimensional view of a simulated amorphous cell of SPX membrane (in the dry state, a) and SPX membrane (in the wet state, b). Interconnected (green) and isolated (red) voids of the SPX membrane (in the dry state, c) and SPX membrane (in wet state, d) illustrated with a probe of 2.4 Å.

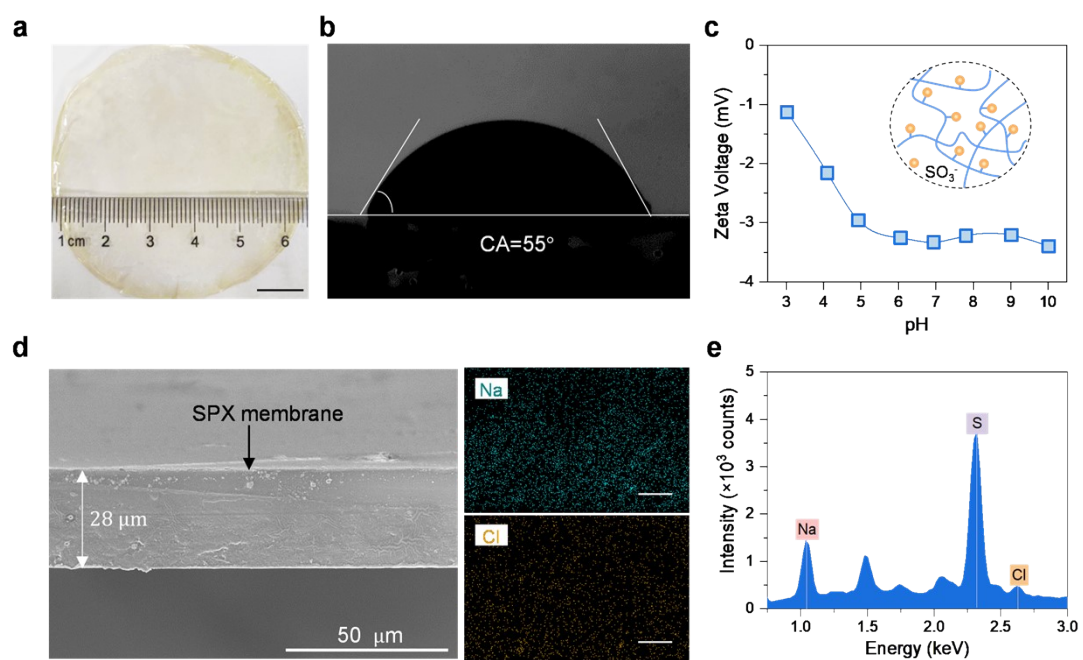


Figure S3. a) Photograph of a SPX membrane sample. scale bar: 1 cm. b) Water contact angle of the SPX membrane. c) Zeta potential values of the SPX membrane under varied pH conditions. The inset shows the negatively charged sulfonated functional groups appended on the polymer backbone. d) Cross-sectional SEM image and the corresponding EDX mapping on element distribution of the SPX membrane after immersed in 1 M NaCl solution (scale bar, 5 μm). e) The element concentration on the cross-section of the SPX membrane.

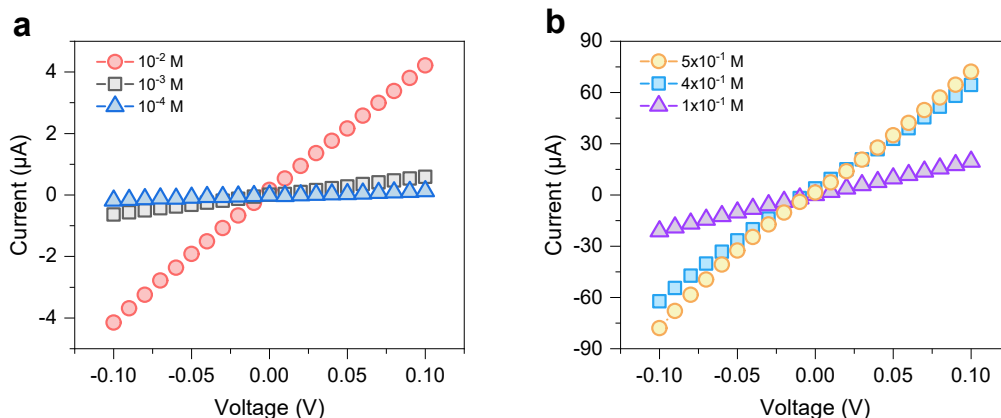


Figure S4. I–V curves recorded for the SPX-based osmotic power generation device in neutral KCl solutions with the concentration range from 10^{-4} M to 0.5 M. Both compartments of the diffusion cell have the same concentration in this case.

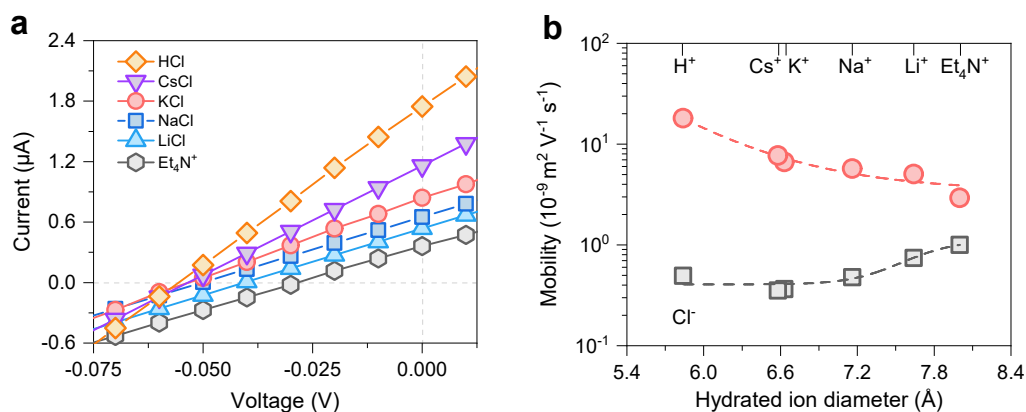


Figure S5. a) I–V curves recorded for the SPX-based osmotic power generation device in various chloride salt solutions under a 10-fold concentration gradient (10 mM/1 mM). b) Cation/proton mobility measured in chloride solutions plotted against the hydrated cation diameter (D_H).

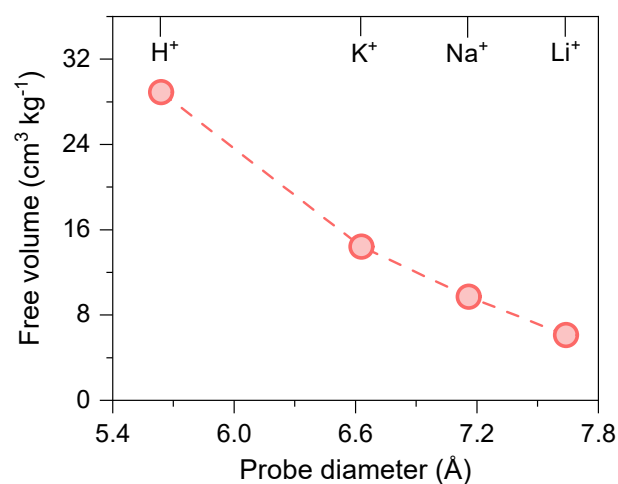


Figure S6. Simulated free volume elements of the SPX matrix with probes having similar size to the selected hydrated cations.

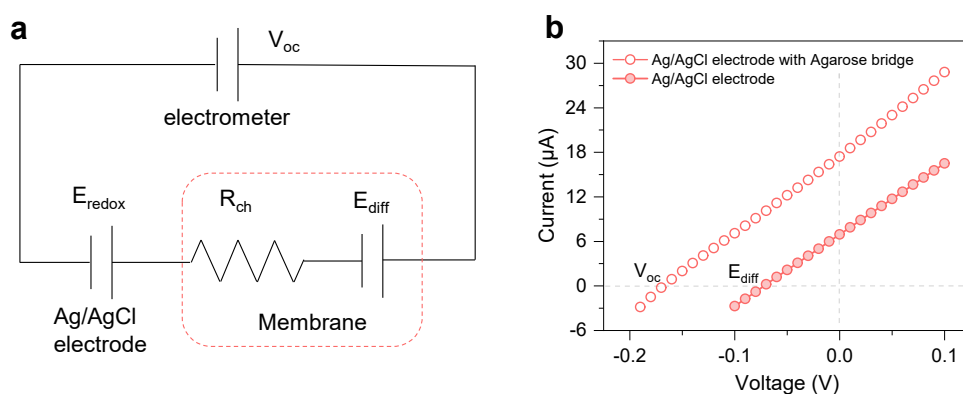


Figure S7. a) The equivalent circuit diagram of the power generator where V_{oc} , E_{redox} , E_{diff} , and R_{ch} represent the measured potential, the redox potential, the diffusion potential contributed by the ion-selective membrane, and the inner resistance of the device, respectively. b) I–V curves recorded for the SPX-based osmotic power generation device under a 50-fold concentration gradient (0.5 M/0.01 M) with Ag/AgCl electrodes directly connected to or connected via salt bridges to the chambers. Both measurements are in good agreement after correction for the theoretical Nernst potential.

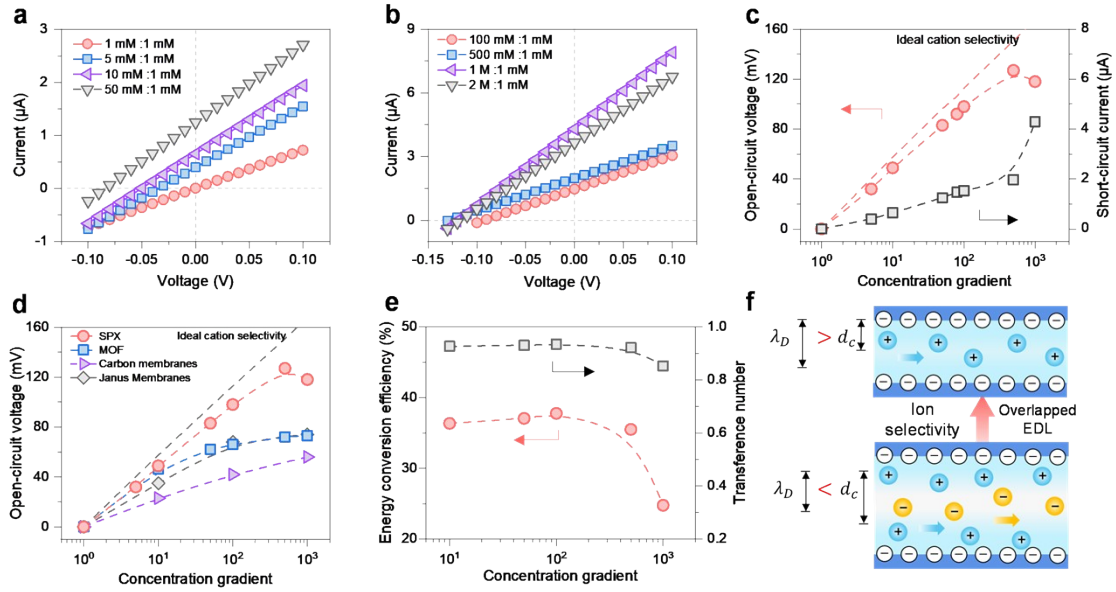


Figure S8. a, b) I–V curves recorded for the SPX-based osmotic power generation device under various concentration gradients. c) The measured open-circuit voltage and short-circuit current under various concentration gradients (the low-salinity solution was fixed at 1 mM NaCl). The dashed line corresponds to the theoretical open-circuit voltage calculated from the Nernst Equation, assuming ideal cation selectivity ($t_+=1$).⁵ d) The open-circuit voltage values are much higher than those from representative osmotic energy conversion systems and close to values calculated from the Nernst equation assuming ideal cation selectivity. e) Energy conversion efficiency and cation transference number under various concentration gradients. f) Schematics explaining the correlation between channel diameter and ion selectivity. The channels exclude all co-ions when the electric double layers overlap (top panel). With a large channel diameter, the insufficient electric double layer overlap leads to poor ion selectivity (bottom panel).

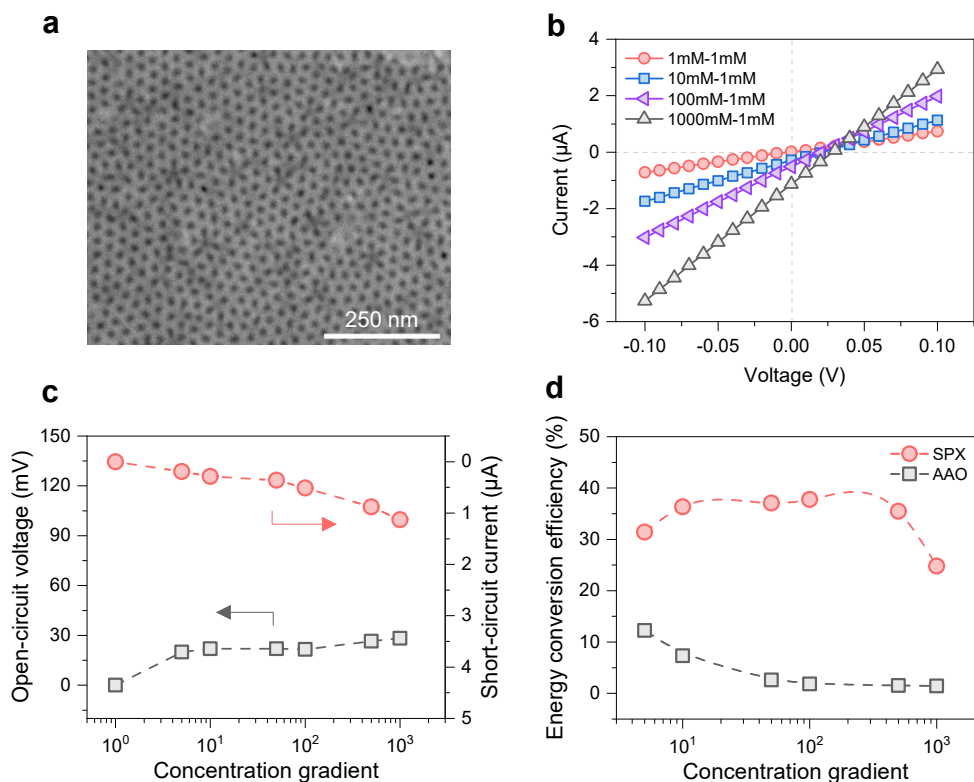


Figure S9. a) SEM image of porous anodic aluminum oxide (AAO) membrane with a channel diameter of about 20 nm. b) I–V curves recorded for the AAO membrane-based device under various concentration gradients. c) The measured open-circuit voltage and short-circuit current of the AAO membrane-based device under various concentration gradients (the low-salinity solution was fixed at 1 mM NaCl). d) Comparing the energy conversion efficiency of SPX-based and the AAO-based osmotic power generation device under various concentration gradients.

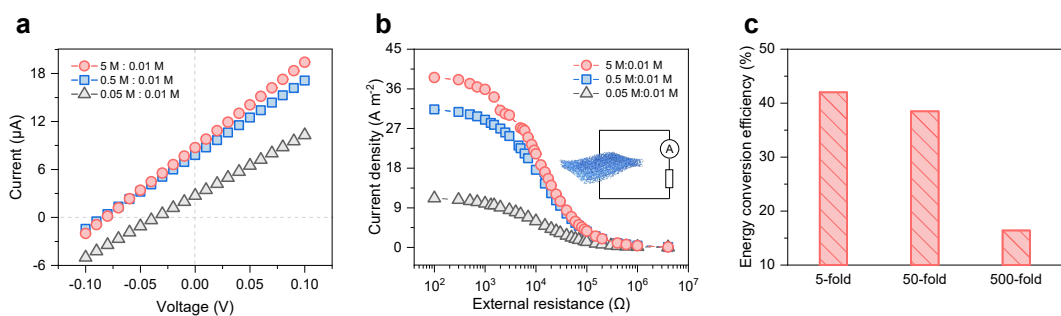


Figure S10. a) I–V curves recorded for the SPX-based osmotic power generation device under three NaCl concentration gradients. b) Current densities of the SPX-based device as functions of load resistance and concentration gradients. c) The energy conversion efficiency under three NaCl concentration gradients.

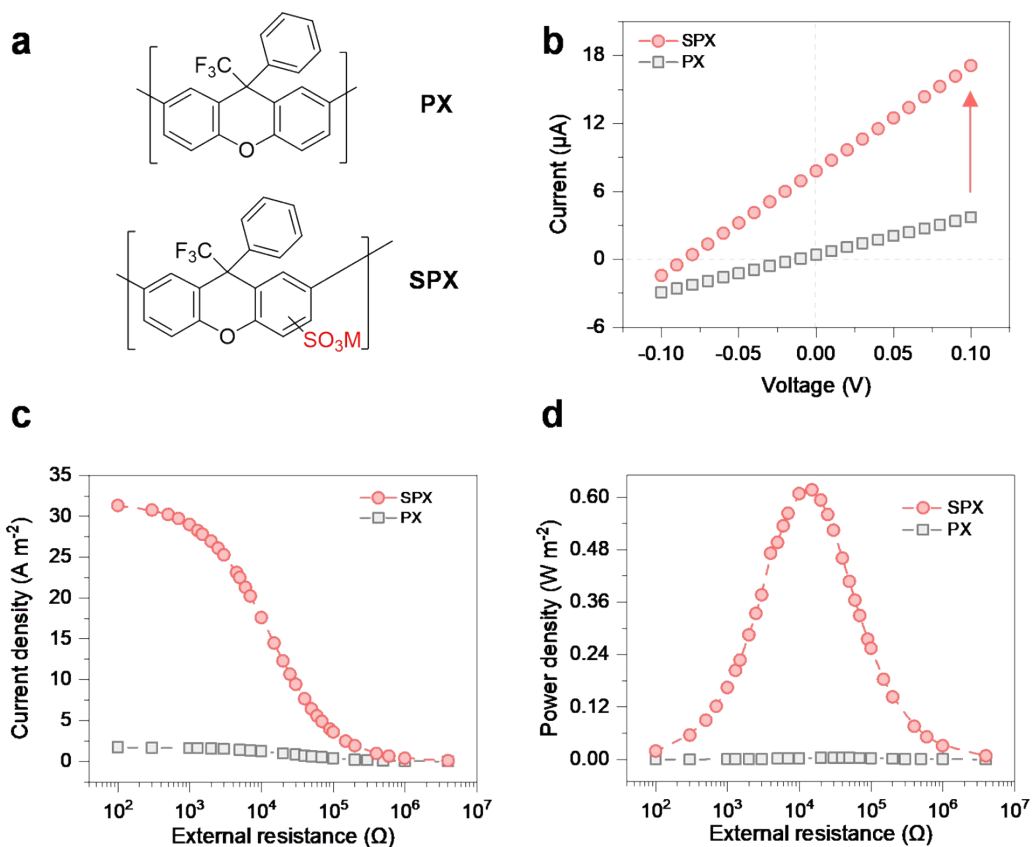


Figure S11 (a) Structure of the polyxanthene-based polymer (PX) and sulfonated polyxanthene-based polymer (SPX). (b) I–V curves recorded for PX and SPX membrane in 0.5 M/0.01 M NaCl solutions. Current densities (c) and power densities (d) as functions of load resistance measured with 0.5 M/0.01 M NaCl solutions.

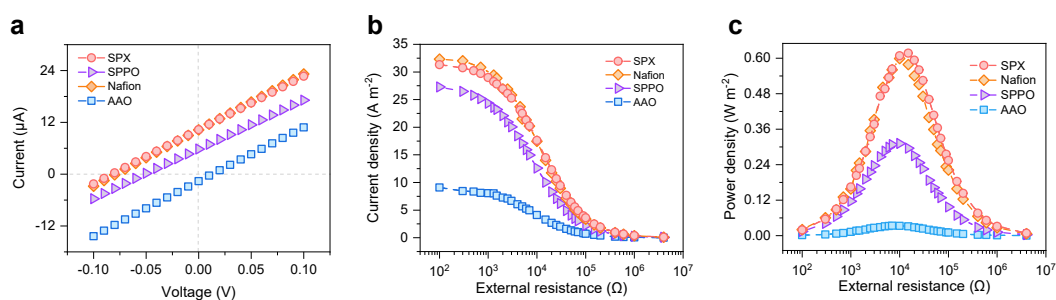


Figure S12. a) I–V curves recorded for various commercial ion-exchange membranes in 0.5 M/0.01 M NaCl solutions. Current densities b) and power densities c) as functions of load resistance measured with 0.5 M/0.01 M NaCl solutions. d) Compared with commercial ion-exchange membranes, the output power density of SPX-based osmotic power generation device reaches a maximum value of 0.62 W m⁻².

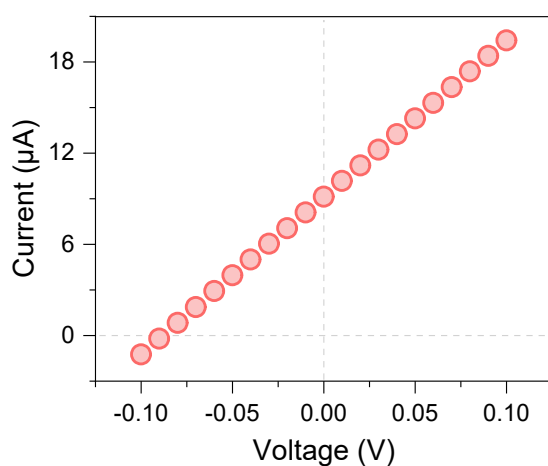


Figure S13. I-V curve recorded for the SPX-based osmotic power generation device under natural river water and seawater (China Bohai Sea water and Huai River water).

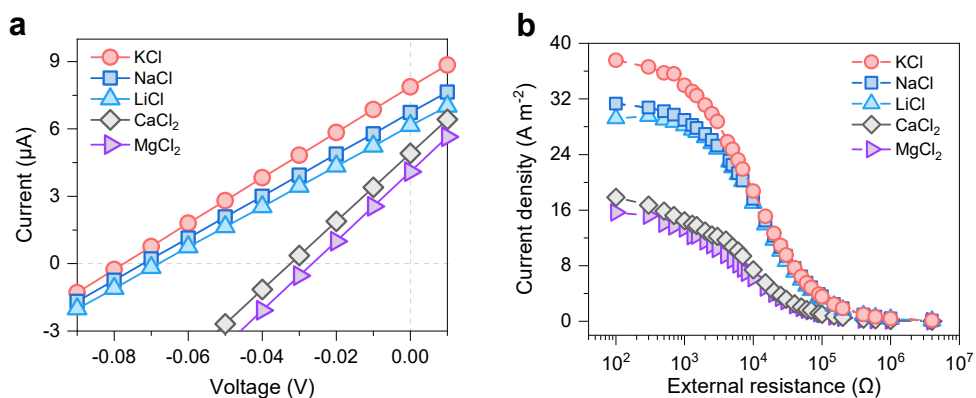


Figure S14. a) I-V curves recorded for the SPX-based osmotic power generation device with various chloride solutions at a fixed concentration gradient of 50 (0.5 M/0.01 M). b) Current densities of the SPX-based device as functions of load resistance in various chloride salt solutions (0.5 M/0.01 M).

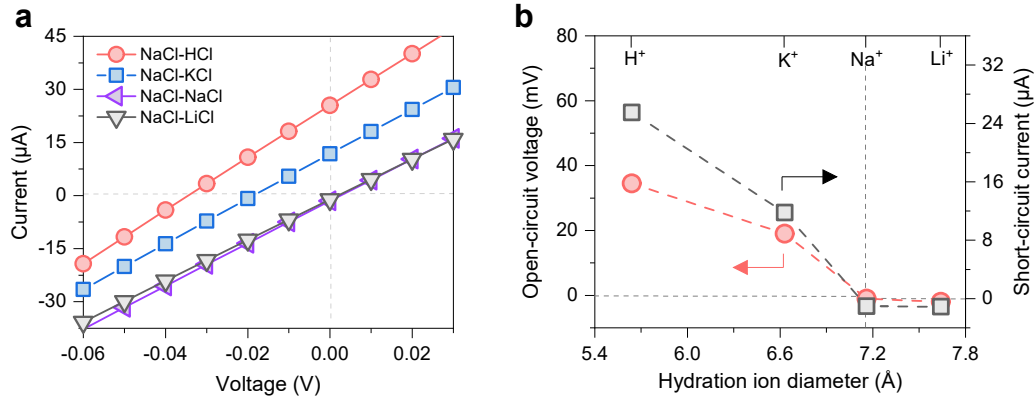


Figure S15. a) I–V curves recorded for the SPX-based osmotic power generator with 0.5 M NaCl/0.5 M XCl (X = H, K, Na, Li) solutions. b) The measured open-circuit voltage and short-circuit current with different salt configurations plotted against hydrated proton/cation diameter.

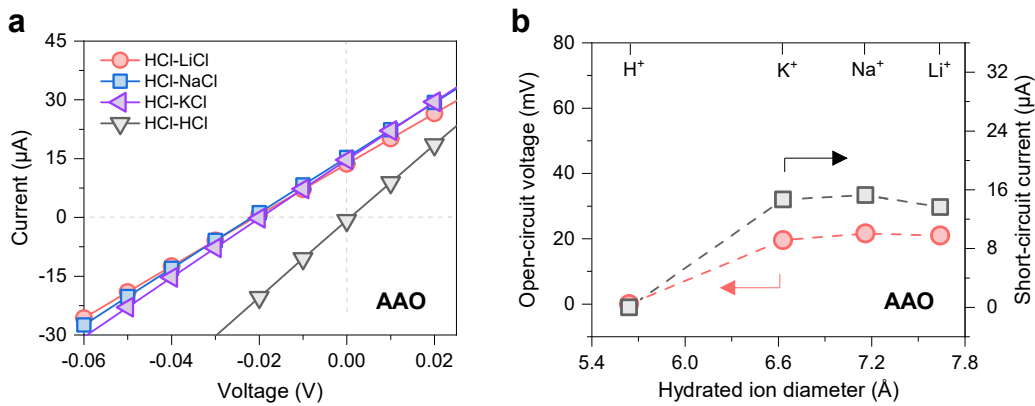


Figure S16. a) I–V curves recorded for AAO membrane in 0.5 M HCl/0.5 M XCl (M=H, K, Na, Li) solutions. b) The measured open-circuit voltage and short-circuit current of AAO membrane with different salt configurations plotted against hydrated proton/cation diameter.

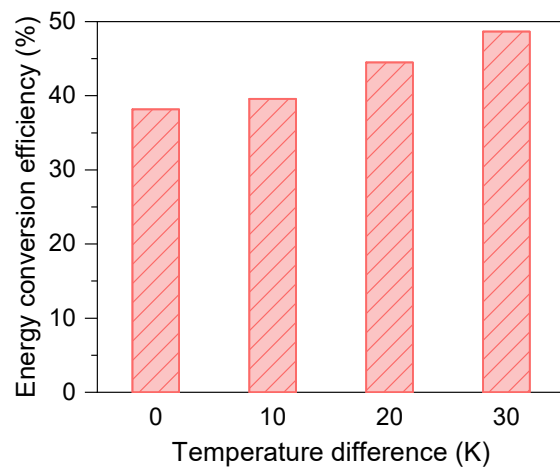


Figure S17. The energy conversion efficiency of the SPX-based osmotic power generator under different temperature differences. The temperature refers to the temperature of the solution.

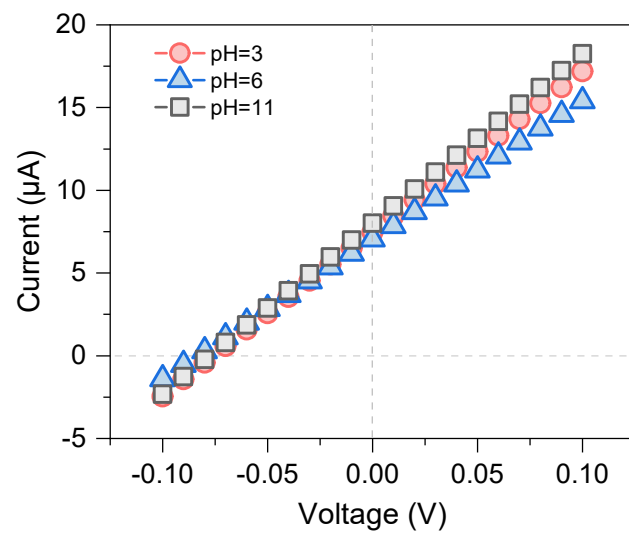


Figure S18. I-V curves recorded for the SPX-based osmotic power generator at different solution pH.

Table S1. The energy conversion efficiencies under various concentration gradients reported/measured for different osmotic power generator.

Material	Thickness	Channel size	Energy conversion efficiency (%)					Power density (W m ⁻²)		Ref.
			10-fold	50-fold	100-fold	500-fold	1000-fold	0.5 M/0.01 M NaCl	0.5 M/0.01 M NaCl	
SPX membrane	30 μm	0.5-0.7 nm	36.3	37.1	37.8	35.5	24.8	38.5	1.23	This work
UiO-66NH ₂ @ANM	750 nm	0.6-0.7 nm	33.0	21.1	17.5	11.9	10.1	-	2.96	18
Ti ₃ C ₂ Tx MXene	2.7 μm	0.64 nm	8.7	-	18.6	-	18.4	-	-	19
GO/SNF/GO	5 μm	0.75 nm	14.6	-	14.3	-	12.4	17.2	5.07	20
TOBC/GO-30	3 mm	0.79 nm	48.0	38.0	35.0	25.0	24.0	38.0	0.53	21
V-GO	350 μm	0.86 nm	8.7	18.7	31.8	23.8	27.4	34.6	10.60	22
N-MXM	8.5 μm	0.68 nm	39.1	-	41.8	-	42.7	-	-	23
P-MXM	8.5 μm	1.07 nm	14.9	-	26.2	-	31.5	-	-	23
MXMs	8.5 μm	-	-	-	-	-	-	44.2	4.60	23
n-GOMs	10 μm	1.01 nm	2.6	-	11.4	-	25.5	-	-	24
p-GOMs	10 μm	0.93 nm	3.9	-	13.0	-	18.6	-	-	24
GOM pairs	10 μm	-	-	-	-	-	-	36.6	0.77	24
HGN membranes	10 nm	1 nm	33.7	-	37.2	-	23.5	-	-	25
MXene membranes	15 μm	1.26 nm	0.4	-	0.3	-	-	45.6	0.53	26
SPEEK/SPSF heterogeneous membrane containing MOF	4.3 μm	1.3 nm	-	-	-	-	-	40	7	27
GO/CNFs	9 μm	1.32 nm	7.8	-	18.4	-	25.1	-	4.19	28
SPEEK membrane	30 μm	2.7 nm	16.7	-	6.6	-	5.5	-	5.80	29
CMWs	75 μm	3.5 nm	35.6	-	36.3	-	34.3	-	2.78	30
Nanoporous carbon-based membranes	2 ± 0.5 nm	3.6 ± 1.8 nm	8.8	-	7.3	-	5.6	-	67.00	31
P-ABC	5 μm	4.48 nm	31.3	28.0	28.0	21.4	22.9	-	-	32
N-ABC	5 μm	2.53 nm	18.3	23.4	24.3	20.5	20.5	-	-	32
BC pairs	5 μm	-	-	-	-	-	-	32	0.23	32
PSS/MOF/AAO	85 μm	5 nm	33.1	-	29.7	-	23.4	29.7	2.87	33
MXene/nanofiber composite membrane	4.5 μm	5-10 nm	2.1	9.0	11.9	17.7	18.2	20.0	3.70	34
Ionic Diode Membrane	64.2 μm	6.7 nm	26.5	-	22.4	-	12.9	37.3	3.46	35
Hydrogel Membrane	24 μm	7 nm	6.2	14.5	14.5	-	11.0	-	5.38	36
Silk Fibroin Membrane	100 nm	7.5 nm	19.2	-	18.6	-	16.8	4.3	4.06	37
MS/AAO	120 nm	8.3 nm	40.7	-	2.0	-	1.0	-	4.50	38
ANF/gel heterogeneous membrane	210 μm	ANFs: 5-10 nm nanofiber: 12 nm	-	-	-	-	-	19.2	3.90	39
Janus Membranes	500 nm	M-1:10 nm M-2:17 nm	17.5	-	16.8	-	9.0	24.3	2.10	40
Janus 3D porous membrane	11 μm	PES-Py:8.5 nm PAEK-HS:17.05 nm	-	-	-	-	-	35.7	2.66	41
Silk-based hybrid membranes	65 μm	20 nm	30.1	-	25.0	-	12.0	17.2	2.43	42
M-MoS ₂ Composite membrane	4 μm	300 nm	-	-	-	-	-	32.0	5.20	43
Hydrogel hybrid membrane	25 μm	-	-	-	-	-	-	14.50	4.08	44
ABN ₃₀ membrane	1 μm	-	7.7	-	7.1	-	4.3	17.3	5.90	45
Polymeric carbon nitride membrane (UFSCNM)	250 nm	-	11.4	-	14.8	10.1	10.4	-	-	46

Table S2. Characteristic parameters of the SPX polymer models.

Species	Density (g cm ⁻³)	Largest free sphere D _F (Å)	Largest included sphere D _I (Å)	Free volume (3.64 Å probe – N ₂ cm ³ kg ⁻¹)
SPX	1.25	2.42	7.79	6.8
SPX-swollen	0.99	4.05	12.07	90.6

Table S3. Performance obtained with the SPX membrane and different commercial ion-exchange membranes. The osmotic energy conversion experimental was conducted at a 50-fold concentration gradient, with 0.5 M NaCl/0.01 M NaCl.

Membrane	Open-circuit voltage (mV)	Short-circuit current (μ A)	<i>t</i> ⁺	Energy conversion efficiency	Power density (W m ⁻²)
SPX	82.20	10.30	0.94	38.8%	0.62
Nafion	78.17	10.27	0.92	35.6%	0.69
SPPO	51.50	5.79	0.78	15.3%	0.31
AAO	12.70	1.72	0.57	0.93%	0.03

Reference

1. P. Zuo, Y. Li, A. Wang, R. Tan, Y. Liu, X. Liang, F. Sheng, G. Tang, L. Ge, L. Wu, Q. Song, N. B. McKeown, Z. Yang and T. Xu, *Angew. Chem. Int. Ed.*, 2020, **59**, 9564–9573.
2. H. J. Zhang, S. Sellaiyan, T. Kakizaki, A. Uedono, Y. Taniguchi and K. Hayashi, *Macromolecules*, 2017, **50**, 3933-3942.
3. S. W. Provencher, *Comput. Phys. Commun.*, 1982, **27**, 213-227.
4. A. Alcaraz, E. M. Nestorovich, M. L. Lopez, E. Garcia-Gimenez, S. M. Bezrukov and V. M. Aguilera, *Biophys. J.*, 2009, **96**, 56-66.
5. A. J. B. a. L. R. Faulkner, *Electrochemical Methods: Fundamentals and Applications*, Wiley, New York, 2001.
6. J. W. Perram and P. J. Stiles, *PCCP*, 2006, **8**, 4200-4213.
7. A. Esfandiari, B. Radha, F. C. Wang, Q. Yang, S. Hu, S. Garaj, R. R. Nair, A. K. Geim and K. Gopinadhan, *Science*, 2017, **358**, 511-513.
8. D.-K. Kim, C. Duan, Y.-F. Chen and A. Majumdar, *Microfluid. Nanofluid.*, 2010, **9**, 1215-1224.
9. G. S. Larsen, P. Lin, K. E. Hart and C. M. Colina, *Macromolecules*, 2011, **44**, 6944-6951.
10. D. Van Der Spoel, E. Lindahl, B. Hess, G. Groenhof, A. E. Mark and H. J. Berendsen, *J. Comput. Chem.*, 2005, **26**, 1701-1718.
11. S. Páll, M. J. Abraham, C. Kutzner, B. Hess and E. Lindahl, *Cham*, 2015.
12. M. J. Abraham, T. Murtola, R. Schulz, S. Páll, J. C. Smith, B. Hess and E. Lindahl, *SoftwareX*, 2015, **1-2**, 19-25.
13. H. J. C. Berendsen, D. van der Spoel and R. van Drunen, *Comput. Phys. Commun.*, 1995, **91**, 43-56.
14. K. E. Hart, J. M. Springmeier, N. B. McKeown and C. M. Colina, *PCCP*, 2013, **15**, 20161-20169.
15. M. J. Frisch, G. W. Trucks, H. B. Schlegel, G. E. Scuseria, M. A. Robb, J. R. Cheeseman, G. Scalmani, V. Barone, G. A. Petersson, H. Nakatsuji, X. Li, M. Caricato, A. V. Marenich, J. Bloino, B. G. Janesko, R. Gomperts, B. Mennucci, H. P. Hratchian, J. V. Ortiz, A. F. Izmaylov, J. L. Sonnenberg, Williams, F. Ding, F. Lipparini, F. Egidi, J. Goings, B. Peng, A. Petrone, T. Henderson, D. Ranasinghe, V. G. Zakrzewski, J. Gao, N. Rega, G. Zheng, W. Liang, M. Hada, M. Ehara, K. Toyota, R. Fukuda, J. Hasegawa, M. Ishida, T. Nakajima, Y. Honda, O. Kitao, H. Nakai, T. Vreven, K. Throssell, J. A. Montgomery Jr., J. E. Peralta, F. Ogliaro, M. J. Bearpark, J. J. Heyd, E. N. Brothers, K. N. Kudin, V. N. Staroverov, T. A. Keith, R. Kobayashi, J. Normand, K. Raghavachari, A. P. Rendell, J. C. Burant, S. S. Iyengar, J. Tomasi, M. Cossi, J. M. Millam, M. Klene, C. Adamo, R. Cammi, J. W. Ochterski, R. L. Martin, K. Morokuma, O. Farkas, J. B. Foresman and D. J. Fox, *Journal*, 2016.
16. M. Pinheiro, R. L. Martin, C. H. Rycroft and M. Haranczyk, *CrystEngComm*, 2013, **15**, 7531-7538.
17. T. F. Willems, C. H. Rycroft, M. Kazi, J. C. Meza and M. Haranczyk, *Microporous Mesoporous Mater.*, 2012, **149**, 134-141.
18. Y. C. Liu, L. H. Yeh, M. J. Zheng and K. C. Wu, *Sci. Adv.*, 2021, **7**, eabe9924.
19. S. Hong, F. Ming, Y. Shi, R. Li, I. S. Kim, C. Y. Tang, H. N. Alshareef and P. Wang, *ACS Nano*, 2019, **13**, 8917-8925.
20. W. Xin, H. Xiao, X. Y. Kong, J. Chen, L. Yang, B. Niu, Y. Qian, Y. Teng, L. Jiang and L. Wen, *ACS Nano*, 2020, **14**, 9701-9710.
21. N. Sheng, S. Chen, M. Zhang, Z. Wu, Q. Liang, P. Ji and H. Wang, *ACS Appl. Mater. Interfaces*, 2021, **13**, 22416-22425.

22. Z. Zhang, W. Shen, L. Lin, M. Wang, N. Li, Z. Zheng, F. Liu and L. Cao, *Adv. Sci.*, 2020, **7**, 2000286.
23. L. Ding, D. Xiao, Z. Lu, J. Deng, Y. Wei, J. Caro and H. Wang, *Angew. Chem. Int. Ed.*, 2020, **59**, 8720-8726.
24. J. Ji, Q. Kang, Y. Zhou, Y. Feng, X. Chen, J. Yuan, W. Guo, Y. Wei and L. Jiang, *Adv. Funct. Mater.*, 2017, **27**, 1603623.
25. H. Wang, L. Su, M. Yagmurcukardes, J. Chen, Y. Jiang, Z. Li, A. Quan, F. M. Peeters, C. Wang, A. K. Geim and S. Hu, *Nano Lett.*, 2020, **20**, 8634-8639.
26. P. Liu, Y. Sun, C. Zhu, B. Niu, X. Huang, X. Y. Kong, L. Jiang and L. Wen, *Nano Lett.*, 2020, **20**, 3593-3601.
27. X. Zhao, C. Lu, L. Yang, W. Chen, W. Xin, X.-Y. Kong, Q. Fu, L. Wen, G. Qiao and L. Jiang, *Nano Energy*, 2021, **81**, 105657.
28. Y. Wu, W. Xin, X.-Y. Kong, J. Chen, Y. Qian, Y. Sun, X. Zhao, W. Chen, L. Jiang and L. Wen, *Mater. Horiz.*, 2020, **7**, 2702-2709.
29. Y. Zhao, J. Wang, X.-Y. Kong, W. Xin, T. Zhou, Y. Qian, L. Yang, J. Pang, L. Jiang and L. Wen, *Natl. Sci. Rev.*, 2020, **7**, 1349-1359.
30. L. Xie, S. Zhou, J. Liu, B. Qiu, T. Liu, Q. Liang, X. Zheng, B. Li, J. Zeng, M. Yan, Y. He, X. Zhang, H. Zeng, D. Ma, P. Chen, K. Liang, L. Jiang, Y. Wang, D. Zhao and B. Kong, *J. Am. Chem. Soc.*, 2021, **143**, 6922-6932.
31. X. Liu, M. He, D. Calvani, H. Qi, K. Gupta, H. J. M. de Groot, G. J. A. Sevink, F. Buda, U. Kaiser and G. F. Schneider, *Nat. Nanotechnol.*, 2020, **15**, 307-312.
32. Z. Wu, P. Ji, B. Wang, N. Sheng, M. Zhang, S. Chen and H. Wang, *Nano Energy*, 2021, **80**, 105554.
33. R. Li, J. Jiang, Q. Liu, Z. Xie and J. Zhai, *Nano Energy*, 2018, **53**, 643-649.
34. Z. Zhang, S. Yang, P. Zhang, J. Zhang, G. Chen and X. Feng, *Nat. Commun.*, 2019, **10**, 2920.
35. J. Gao, W. Guo, D. Feng, H. Wang, D. Zhao and L. Jiang, *J. Am. Chem. Soc.*, 2014, **136**, 12265-12272.
36. W. Chen, Q. Wang, J. Chen, Q. Zhang, X. Zhao, Y. Qian, C. Zhu, L. Yang, Y. Zhao, X. Y. Kong, B. Lu, L. Jiang and L. Wen, *Nano Lett.*, 2020, **20**, 5705-5713.
37. J. Chen, W. Xin, X.-Y. Kong, Y. Qian, X. Zhao, W. Chen, Y. Sun, Y. Wu, L. Jiang and L. Wen, *ACS Energy Lett.*, 2019, **5**, 742-748.
38. S. Zhou, L. Xie, L. Zhang, L. Wen, J. Tang, J. Zeng, T. Liu, D. Peng, M. Yan, B. Qiu, Q. Liang, K. Liang, L. Jiang and B. Kong, *ACS Appl. Mater. Interfaces*, 2021, **13**, 8782-8793.
39. Z. Zhang, L. He, C. Zhu, Y. Qian, L. Wen and L. Jiang, *Nat. Commun.*, 2020, **11**, 875.
40. Z. Zhang, X. Sui, P. Li, G. Xie, X. Y. Kong, K. Xiao, L. Gao, L. Wen and L. Jiang, *J. Am. Chem. Soc.*, 2017, **139**, 8905-8914.
41. X. Zhu, J. Hao, B. Bao, Y. Zhou, H. Zhang, J. Pang, Z. Jiang and L. Jiang, *Sci. Adv.*, 2018, **4**, eaau1665.
42. W. Xin, Z. Zhang, X. Huang, Y. Hu, T. Zhou, C. Zhu, X. Y. Kong, L. Jiang and L. Wen, *Nat. Commun.*, 2019, **10**, 3876.
43. C. Zhu, P. Liu, B. Niu, Y. Liu, W. Xin, W. Chen, X. Y. Kong, Z. Zhang, L. Jiang and L. Wen, *J. Am. Chem. Soc.*, 2021, **143**, 1932-1940.
44. W. Chen, Q. Zhang, Y. Qian, W. Xin, D. Hao, X. Zhao, C. Zhu, X.-Y. Kong, B. Lu, L. Jiang and L. Wen, *ACS Cent. Sci.*, 2020, **6**, 2097-2104.
45. C. Chen, D. Liu, L. He, S. Qin, J. Wang, J. M. Razal, N. A. Kotov and W. Lei, *Joule*, 2020, **4**, 247-261.

46. K. Xiao, P. Giusto, L. Wen, L. Jiang and M. Antonietti, *Angew. Chem. Int. Ed.*, 2018, **57**, 10123-10126.